crystals

MDPI

Article

First-Principles Calculation and Analysis of the Magnetic and Mechanical Properties of Mo_2C with Vacancy Defects and Substitutional Doping

Xiaoliang Qing [1], Jing Guo [2], Xiaoxiao Liu [1], Qian Zhang [1], Tammam Kaid [1], Nathan Outterside [1], Cong Tang [1], Li Wang [3], Qingxiang Yang [4,*] and Xuejun Ren [1,*]

[1] School of Engineering, Liverpool John Moores University, Liverpool L3 3AF, UK; x.qing@2020.ljmu.ac.uk (X.Q.); x.liu@ljmu.ac.uk (X.L.); q.zhang@ljmu.ac.uk (Q.Z.); t.kaid@2016.ljmu.ac.uk (T.K.); n.outterside@2020.ljmu.ac.uk (N.O.); ctang3@jaguarlandrover.com (C.T.)
[2] Department of Materials, The University of Manchester, Manchester M13 9PL, UK; jing.guo-2@manchester.ac.uk
[3] School of Engineering and Materials Science, Queen Mary-University of London, London E1 4NS, UK; l.i.wang@qmul.ac.uk
[4] State Key Laboratory of Metastable Materials Science and Technology, Yanshan University, Qinhuangdao 066104, China
* Correspondence: qxyang@ysu.edu.cn (Q.Y.); x.j.ren@ljmu.ac.uk (X.R.)

Abstract: In this study, the first-principles method is adapted to establish key data for β-Mo_2C with various point defects. A particular focus is comparatively studying the effects of point vacancies and different substitutional doping elements on the structures and electronic, magnetic and mechanical properties of β-Mo_2C. The calculation results show that vacancy defects and substitutional doping have different impacts on the magnetism and bulk modulus of Mo_2C. Data for the effect of different substitutional doping elements (V, Cr, Co, Fe, Ni and W) on the physical and mechanical properties/behaviours are established and analysed. The changes in key magnetic properties (local and total magnetic moments) associated with different point substitutional doping elements are comparatively analysed with reference to the data of Mulliken atomic charge, bond population, density of states (DOS) and band structures. The correlation between doping elements and changes in magnetic moment and bulk modulus is discussed. The influence of doping elements on the magnetic moment of 3D Mo_2C is also compared to their effects on a two-dimensional Mo_2C monolayer. The potential applications of DFT modeling and data for future research and development related to materials and processing are discussed.

Keywords: carbides; defects; vacancies; substitutional doping; magnetism

Academic Editor: John A. Mydosh

Received: 25 November 2024
Revised: 10 December 2024
Accepted: 21 December 2024
Published: 30 December 2024

Citation: Qing, X.; Guo, J.; Liu, X.; Zhang, Q.; Kaid, T.; Outterside, N.; Tang, C.; Wang, L.; Yang, Q.; Ren, X. First-Principles Calculation and Analysis of the Magnetic and Mechanical Properties of Mo_2C with Vacancy Defects and Substitutional Doping. *Crystals* **2025**, *15*, 33. https://doi.org/10.3390/cryst15010033

1. Introduction

First-principles calculations are an important tool for establishing data on compounds in different forms including both 3D and 2D structures with defects [1–8]. Many research works have reported the use of them for investigating the effects of defects on the structure and properties of different compounds. For example, Razumovskiy et al. [2] explored the formation and interaction of point defects in group IV_b transition metal carbides and nitrides while Zhang et al. [5] studied carbon-vacancy ordering in Nb_4AlC_{3-x}. Recently, Bai et al. [7] reported a predictive study on the role of carbon vacancies in determining the structural, mechanical and thermodynamic properties of $(HfTaZrNb)C_{1-x}$ high entropy carbides. In another recent work, Bie et al. [8] studied sub-stoichiometry and vacancy structures in V/Nb carbide precipitates using cluster expansion and first-principles calculations.

First-principles calculations have also been widely used as an effective tool for predicting and studying the effects of doping elements [9–12]. In the work by Cao et al. [9], first-principles calculations were used to study enhanced N_2 fixation on V_2C by transition metal doping. Cheng et al. [10] investigated the electronic and magnetic properties of Au-doped diamond surfaces. Some work has also used data from first-principles calculation to develop insights into the evolution of key phases in complex alloys such as precipitated carbides and the design of high-performance multicomponent carbides [10–13]. Feng et al. [12] reported the effect of Cr atom doping on carbide stability and mechanical properties of high-carbon chromium-bearing steels. The results showed that the doping of Cr contributed to the movement of metal atoms to change from translation to rotation during the transformation of the carbide. A recent work [10] reported the formation mechanism of multicomponent carbides (Nb, M)C (M = Ti, Cr and Mn) and correlated the finding with advanced experiments, including transmission electron microscopy (TEM) and three-dimensional atom probe tomography (3D-APT).

The process and analysis results from first-principles calculations can be complex as different data sets of properties and structures can be interlinked, particularly for complex material groups [14–19]. TMCs have found wide applications due to their mechanical, thermal and magnetic properties. Typical beneficial characteristics of TMCs include high melting points, hardness and extremely high thermal and mechanical stability, making them suitable for applications such as cutting tools, nuclear reactors and catalysts [3,20–23]. Molybdenum carbide is a typical example of TMC with different forms and applications across different areas. Mo_2C is also an important precipitate in different steels and alloys containing Fe, Cr, Ni, etc. [21,24–29]. Molybdenum carbide has different phases and structures including γ-MoC, β-Mo2C, and γ′ [29]. γ-MoC is isostructural with tungsten carbide (WC) and exhibits a simple hexagonal structure with an AAAA packing. γ′-MoC phase with an AABB stacking of the metal planes. Yang et al. [22] also calculated the surface energy of the α-Mo_2C (023) plane and found that the Y doping can facilitate electron escape from the α-Mo_2C (023) surface, resulting in enhanced surface activities. The electronic structure and catalytic functions of Mo_2C are reported to be similar to those of the precious metal Pt, which made Mo_2C with different doping suitable for a range of important applications in 2D materials, energy storage, superconductivity and catalysis [26–28]. In recent work, Guo et al. [3] reported first-principles calculations of energy and structure of the point defects, vanadium-related defects and defect combinations. In this study, previous work is extended to comparatively investigate the effects of point vacancies and substitutional doping of a range of elements on magnetic properties and relationships between different data sets from DFT calculations. Data on structural, electronic and magnetic properties, including band population, charge redistribution, DOS and band structures, are established and analysed with respect to magnetic and other properties. The correlation between magnetic moments of doping elements and bulk modulus is also analysed. Finally, the relationship between magnetic moment in bulk 3D and 2D Mo_2C structures with similar point defects and doping elements is also examined. The effect of point vacancy and doping elements on different properties, along with the interplay between different types of data and future development, is discussed.

2. Calculation Details and Data Development

2.1. Models of Point Defects and Substitutional Doping

This work is focused on presenting and analysing some key data related to molybdenum semi-carbide (β-Mo_2C) with point vacancies and substitutional doping, including the formation energy of point defects, lattice parameters of relaxed structures, magnetic moments, electronic data and key mechanical properties. The unit cell and a typical super-

cell are shown in Figure 1. Mo_2C belongs to the hexagonal crystal system P-3m1 (Z = 1) with initial lattice constants of the base cell being a = b = 3.073 Å and c = 4.653 Å. The unit cell contains two effective Mo atoms and one C atom at different positions. As shown in Figure 1c, Mo_2C supercell exhibits a layered structure. The distance between Mo and C atomic layers within each layer is about half of the nearest distance between the adjacent two Mo atomic layers. Figure 2 shows the models with the sites for C vacancy (V_C) and Mo vacancy (V_{Mo}). In each case, one atom of C or Mo is removed from the supercell, followed by structural relaxation as in [3].

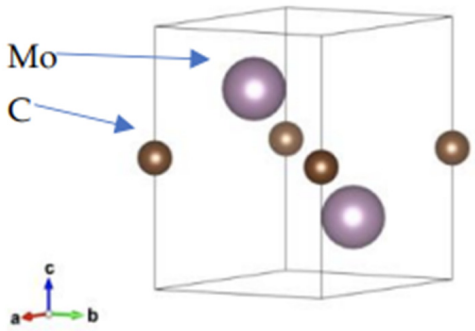

(**a**) Unit cell of pristine Mo_2C.

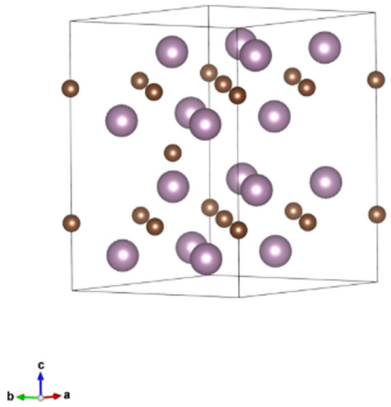

(**b**) Typical example of a supercell of Mo_2C.

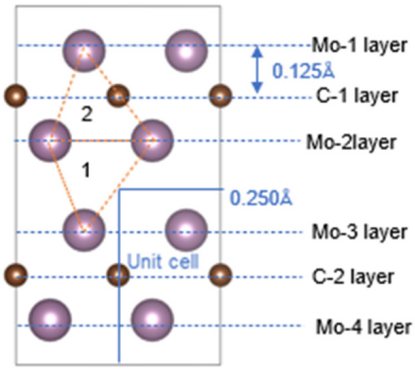

(**c**) Side view of the supercell model and illustration of the Mo-C-Mo layered structure within the crystal.

Figure 1. Crystal structures of Mo_2C model (**a**), typical supercell (**b**) and layered structure (**c**).

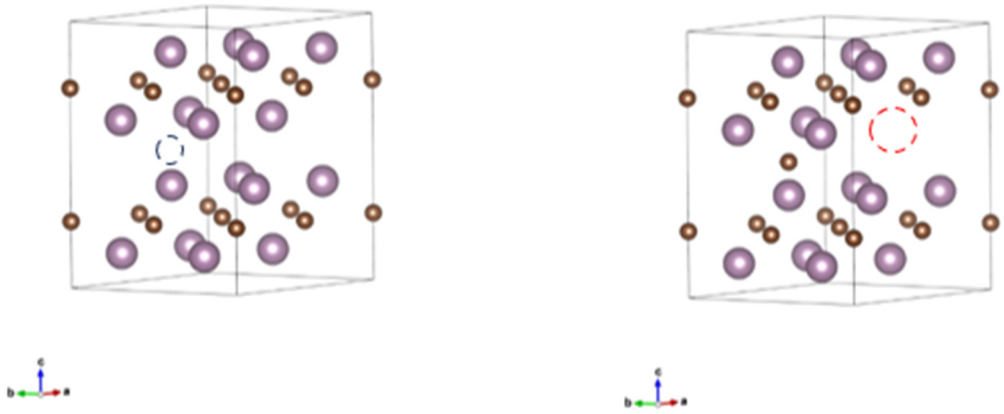

(**a**) C-Vacancy (the carbon atom is removed from the supercell indicated by the blue open circle)

(**b**) Mo-Vacancy (the Mo atom is removed from the supercell indicated by the red open circle)

Figure 2. Typical models with different vacancy defects: (**a**) C-vacancy, (**b**) Mo-Vacancy.

Figure 3 shows substitutional doping with different elements. The selected doping elements for analysis include Vanadium (V), Nickel (Ni), Chromium (Cr), Iron (Fe), Cobalt (Co) and Tungsten (W). These elements have been reported in the doping of different carbide systems or co-exist in alloys with Mo_2C [23,30–32]. Normally, doping-related defects in carbides contain two different types, one is substitutions and the other is interstitials. This study focuses on substitutional doping, where the doping element occupies the Mo atom site directly. Substitutional doping is a common form in TMCs, and gaining an improved understanding of their roles through a comparative study is important for optimising their properties, understanding underlying mechanisms, and advancing their applications [3,33–35].

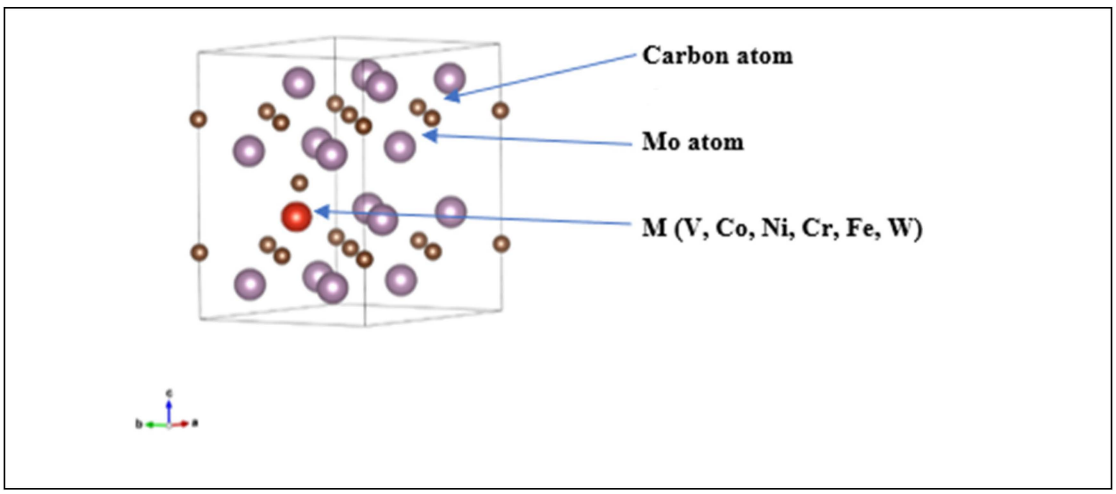

Figure 3. A typical model showing substitutional doping on Mo site with Metal elements (M = V, Co, Ni, Cr, Fe, W).

2.2. Main Calculation and Data Development

In this study, all calculations were performed using a first-principles approach based on density functional theory (DFT), implemented in the Vienna Ab initio Simulation Package (VASP) [36]. Some analyses were also performed using CASTEP for comparison and to effectively develop systematic data such as Mulliken atomic charge and bond population in the supercell with different defects. The comparative use of VASP and CASTEP is effective for data system development and offers reliable cross-examination of the data with a

predictive nature. The exchange–correlation functional was described by the Perdew–Burke–Ernzerhof (PBE) generalized gradient approximation (GGA), which is a widely used and reliable density functionals for simulating solid materials, including TMCs and other types of intermetallic compounds. Structure optimisation was performed using the Broyden–Fletcher–Goldfarb–Shanno (BFGS) algorithm. The energy, maximum force and maximum displacement were set as 5×10^{-6} eV/atom, 0.01 eV/Å and 5×10^{-4} Å for the convergence tolerances, respectively. Detailed convergence tests have been performed following a similar procedure as in previous work [3]. The Monkhorst–Pack k-point samplings of $6 \times 6 \times 6$ and a plane–wave cutoff energy of 380 eV were used for the Mo_2C unit cell. As an important part of the data development process, a range of supercells of different sizes were built and optimised (from $1 \times 1 \times 1$ (3 atoms) to $3 \times 3 \times 3$ (81 atoms)). Given that the data development and analysis are focused on point defects, a 24-atom supercell with a $2 \times 2 \times 2$ unit cell was chosen in the main calculations, which is effective in balancing the accuracy and efficiency of the calculation for comparative studies. All structures were fully relaxed until the total energy converged to within 10^{-7} eV. The accuracy and approach employed for the supercell calculations are consistent with those reported in similar studies [26,37,38].

In the general framework of VASP, Schrödinger's equation is solved to simultaneously capture thermodynamic properties, electronic behaviour and atomic structure (Equation (1))

$$\left[-\frac{\hbar^2}{2m_c}\nabla_i^2 + v_{\text{eff}}\right]\psi_i = \varepsilon_i\psi_i \tag{1}$$

DFT utilise the electron density functional to enhance the calculation efficiency when solving Schrödinger's equation:

$$E[n] = T[n] + E^H[n] + E^{XC}[n] + \int V\left(\vec{r}\right)n\left(\vec{r}\right)d^3r \tag{2}$$

where $T[n]$ is Kinetic energy, $E^H[n]$ is Hartree energy and $\int V\left(\vec{r}\right)n\left(\vec{r}\right)d^3r$ is potential energy. $E^{XC}[n]$ is exchange–correlation energy, which is the main component linked to the local spin density (LSD) or the generalized gradient approximation (GGA).

In the commonly used PBE model [39], Perdew–Burke–Ernzerhof defined the enhancement factor, F_{XC}, over local exchange to depict the nonlocality of the GGA (Equation (3)):

$$E_{XC}^{GGA}[n_\uparrow, n_\downarrow] = \int d^3r n\epsilon_X^{\text{unif}}(n)F_{XC}(r_s, \zeta, s) \tag{3}$$

This equation represents any GGA exactly when the spin polarization ζ is constant with respect to r. In cases where ζ varies, the equation remains approximately valid. Further details of theoretical frames could be referred to [36,40].

2.3. Main Structure and Property Data

Vacancy and substitutional defects could affect many properties and behaviours. This analysis focuses on formation energy of the defects, optimised lattice parameters, local lattice distortion, Mulliken atomic charge and bond population and total/local magnetic moments. The relationship between magnetic properties and bulk modulus is also analysed. The magnetic moment data for the bulk model are compared with selected first-principles calculation data of the 2D Mo_2C structure. The electronic structure calculations, including the density of states and band structure, were central to this analysis. The DOS was decomposed into contributions from different atomic orbitals to understand the role of each element and orbital in the electronic properties. Band structures were computed along high-symmetry directions in the Brillouin zone to identify the electronic bandgap

and potential bonding behaviour. The density of states and band structures data are correlated with changes in magnetic moment and bulk modulus of Mo_2C with different doping elements. Magnetic data were comprehensively described using spin-polarized DFT explicit treatment of electron spin, enabling the calculation of spin density and magnetic moments. Spin density is defined as the difference in electron density between spin-up and spin-down states, providing a direct measure of magnetic moment distribution. All spin-polarized calculations were performed using the projector-augmented wave (PAW) method to describe the interaction between ions and electrons [40]. The exchange-correlation energy was treated using the generalized gradient approximation (GGA) parameterised by Perdew, Burke and Ernzerhof (PBE) [39]. Partial magnetic moments were also decomposed into contributions from the s, p and d orbitals of Mo atoms and the corresponding doped transition metal (TM) atom. This decomposition provides detailed insights into the orbital-specific contributions to the local and overall magnetic moment. As part of the data development process, elastic properties of Mo_2C both with/without defects were also calculated. The elastic properties also provide useful data for validation and correlation with the magnetic properties [41–43].

Given the predictive nature of this comparative study of point defects and doping, the lattice structure and properties of pristine Mo_2C carbide were computed to assess the reliability of the DFT methodology and following similar comparative studies [13]. The lattice parameters and volume of the optimised Mo_2C unit cell were compared to different published sources [23,44,45]. The value for bulk modulus is 291 GPa (Voigt model), 290 GPa (Reuss model) and 190 GPa (Hill model), which show good agreement with average data from other published sources [23,45]. Similar cross-examination of the approach was performed by comparing the DFT data of other related compounds of similar nature with published data (Nickel carbides (NixC (x = 1–4), TiC, V_2C, Cr_2C, Fe_2C) [43]. Further discussion will be presented with the results and discussions.

3. Main Calculation, Results and Data Analysis

3.1. Defect Formation Energy and Structure

The formation energy (Edef) of point defects is defined as:

$$\mathrm{Edef} = \mathrm{E(N)} - \mathrm{Eperf(N)} + \mathrm{E(A)} - \mathrm{E(B)} \quad (4)$$

where E(N) is the total energy of the supercell containing the defect; E_{perf}(N) is the total energy of the ideal supercell; E(A) is the energy of the replaced or deleted atom; and E(B) is the energy of the added substituting atom relative to the ideal supercell. Table 1 summarises the formation energies of point defects within the Mo_2C lattice, including vacancies of a single Mo atom (V_{Mo}) and a single carbon atom (V_C); and substitutional atoms for replacing molybdenum sites ($S_{M\text{-}Mo}$, M = V, Co, Ni, Cr, Fe, or W). The lattice parameter after relaxation is also presented in Table 1, the value for the pristine Mo_2C cell (3.049; 3.049; 4.662) is in agreement with published experimental data and other theoretical analyses [6,44]. The data show that vacancy defects lead to a decrease in lattice parameters and volume, which agrees with the general effect of vacancies reported in the literature [7,46]. As shown by the data, the formation energy of the vacancy defect (V_{Mo} and V_C) is higher than the formation energy of substitutional doping. The formation energy varies among the substitution doping elements and the doping elements exhibit different degrees of lattice deformation. Tungsten ($S_{W\text{-}Mo}$) has the lowest formation energy, followed by nickel ($S_{Ni\text{-}Mo}$), vanadium ($S_{V\text{-}Mo}$), chromium ($S_{Cr\text{-}Mo}$), iron ($S_{Fe\text{-}Mo}$) and cobalt ($S_{Co\text{-}Mo}$). The negative values for $S_{W\text{-}Mo}$, $S_{Ni\text{-}Mo}$, $S_{V\text{-}Mo}$ and $S_{Cr\text{-}Mo}$ suggest that these doping elements are favourable under certain synthesis conditions. The data indicate that tungsten doping ($S_{W\text{-}Mo}$) contributes to

structural stability with limited expansion in all three directions, while iron doping may be associated with significant contraction.

Table 1. Formation energy (eV) of point defects for Mo_2C and key dimensions of the relaxed structure.

Supercell	Formation Energy and Dimensional Parameters	
	Formation Energy of Point Defect	**Dimensions (a, b, c) (After Structure Relaxation)**
Perfect/Pristine Mo_2C		3.0491, 3.049, 4.662
V_{Mo}	0.5961	3.041, 3.041, 4.629
V_C	3.5	3.029, 3.029, 4.647
$S_{V\text{-}Mo}$	−0.53	3.043, 3.043, 4.654
$S_{Fe\text{-}Mo}$	0.499	2.627, 2.627, 4.051
$S_{W\text{-}Mo}$	−3.54	3.053, 3.053, 4.675
$S_{Cr\text{-}Mo}$	−0.1618	3.042, 3.042, 4.654
$S_{Ni\text{-}Mo}$	−0.8324	3.049, 3.049, 4.644
$S_{Co\text{-}Mo}$	0.8828	3.049, 3.049, 4.636

Data on the Mulliken population and bond population are relevant to both magnetic and mechanical properties, which can be used to analyse the charge transfer and chemical bonding characteristics, including electron charge around the atom and the overlap between the two bonding atoms [15,47,48]. The Mulliken charge measures effective valence from the absolute difference between formal ionic charge and Mulliken charge on atomic species. In CASTEP, population analysis is performed with a projection of the plane–wave (PW) states onto a linear combination of atomic orbitals (LCAO) localized basis, with population analysis of the resultant projected states following the Mulliken formalism [47] The main output from the analysis includes a Mulliken charge and bond population, both influence bond strength.

The Mulliken atomic charge is based on the net charge of each atom, which comes from the sum of the nuclear charge minus the electron density, including self-energy electrons and shared electrons:

$$Q_A = Z_A - \sum_\mu P^A_{\mu\mu} - \frac{1}{2}\sum_{\mu\neq\nu} P^A_{\mu\nu} \quad (5)$$

where Q_A is the Mulliken atomic charge of atom A; Z_A is the nuclear charge number (i.e., atomic number) of atom A; $P\mu\mu$ represents the electron density in the orbit of atom A itself; and $P\mu\nu$ represents the electron density shared by atom A with other atoms.

The bond population is determined by their orbital overlap and electron density distribution. The bond overlap population between atoms A and B (P_{AB}) can be expressed as:

$$P_{AB} = \sum_{\mu\in A}\sum_{\nu\in B} P_{\mu\nu}S_{\mu\nu} \quad (6)$$

$P\mu\nu$ is the electron density matrix value between the orbitals of atoms A and B.

$S\mu\nu$ is the overlap matrix value between orbitals.

The bond population also reflect the bond strength between the two atoms. The higher the bond overlap population value, the stronger the covalency of the bond; if the value is negative, there may be an anti-bonding effect.

The calculation needs to be summed over all the key points following the process below.

The Mulliken charge associated with a given atom, A, can be determined as:

$$Q(A) = \sum_k \omega_k \sum\sum_\mu^{onA}\sum_\nu P_{\mu\nu}(k)S_{\mu\nu}(k)\sum \quad (7)$$

In the equation, k refers to all K points, ω_k is the weighting and $P_{\mu\nu}$ (k) is the density matrix. $S_{\mu\nu}$(k) represents the overlap matrix between orbitals. The bond population between two atoms A and B over different K points can be then calculated as:

$$P(AB) = \sum_k \omega_k \sum \sum_{\mu}^{onA} \sum_{v}^{onB} 2P_{\mu v}(k) S_{\mu v}(k) \quad (8)$$

Table 2 lists the Mulliken atomic charge and bond population in the supercell with different defects. The bond population is an indication of bond covalency in a crystal, where a high value of bond population in essence indicates a high degree of covalency in the chemical bond, which could affect electronic, magnetic and mechanical properties. Bond populations indicate bond strength, with higher values suggesting stronger covalent character. The effect of point defects could be analysed by comparing the data with that of the Mo-C bond population in a perfect Mo_2C lattice, which is 0.33. For molybdenum vacancy (V_{Mo}), the Mo-C bond populations around the Mo vacancy increase significantly, with values up to 0.51. This rise suggests an increased bonding interaction between C atoms compensating for the missing Mo atom, enhancing stability near the vacancy. For C-Vacancy (V_C), it shows that the Mulliken atomic charge of Mo atoms near the vacancy is decreased, which suggests weakened Mo-Mo interactions in the absence of C, as C atoms contribute to Mo's stable coordination environment.

Table 2. Mulliken atomic charge and bond population in the supercell with different defects. (All Mo-C bond populations in the pristine Mo_2C are 0.33, and the Mulliken atomic charge for Mo and C atoms in the pristine Mo_2C is 0.3 and −0.6, respectively.)

Defect	Atomic Charge (e)			Bond Population	
	Mo	C	M-C	Mo-C Bond	Doping M-C Bond
V_{Mo}	0.36, 0.27, 0.01	−0.61, −0.54	—	0.51, 0.43, 0.34, 0.29, 0.27, 0.13	—
V_C	0.25, 0.27	−0.59	—	0.41, 0.33, 0.29	—
$S_{V\text{-}Mo}$	0.20, 0.26	−0.61	0.67	0.38, 0.32	0.23
$S_{W\text{-}Mo}$	0.35, 0.33, 0.24	−0.64	0.3	0.35, 0.33, 0.32	0.39
$S_{Fe\text{-}Mo}$	0.33, 0.24, 0.19	−0.6, −0.57	0.6	0.41, 0.36, 0.33, 0.24	0.28
$S_{Cr\text{-}Mo}$	0.32, 0.31, 0.29	−0.59, −0.57	0.17	0.34, 0.33, 0.31	0.37
$S_{Ni\text{-}Mo}$	0.35, 0.33, 0.224	−0.6, −0.57	−0.47	0.35, 0.33, 0.23	0.23
$S_{Co\text{-}Mo}$	0.32, 0.29, 0.27	−0.59, −0.58	0.58	0.41, 0.35, 0.33, 0.26	0.21

Substitutional doping elements exhibit a diverse effect on the Mulliken atomic charge of Mo, C and M-C. There is limited change in the charge value for Mo and C in most cases; however, for vanadium (V), the charge is relatively high, and similar elevated values are observed for iron (Fe) and cobalt (Co). In contrast, nickel (Ni) has a negative value, while chromium (Cr) and tungsten (W) exhibit moderate values. Compared to the pristine Mo_2C structure, carbon atoms in doped structures, such as those with W and Ni, lose more electrons. When comparing the Mo-C and the M-C bond populations, V, Fe and Co substitution shows a higher Mo-C bond population, while Cr, W and Ni substitution yields moderate bond populations around 0.34, close to the value of 0.33 in the pristine structure. The bond population for doping the M-C pair also shows the differences between the M-elements, with W displaying a much higher value. These variations provide insights into the material's properties. For example, the close similarity of all the key data between W and Mo suggests that W integrates well into the Mo site, maintaining a similar electronic environment without causing significant charge imbalance. The bond populations for W-C bonds are relatively high, around 0.39, indicating strong

W-C bonding. This strong bonding, combined with W's high covalency and atomic weight, is associated with enhanced magnetic and bulk modulus, which will be further discussed in the discussion section.

3.2. Magnetic Data and Analysis

Figure 4 shows the data for magnetic moments (per unit cell) for various structures. The magnetic moment magnitude of an atom is described as the difference between the spin-up and spin-down state density integral below the Fermi level. The total magnetic moment (MM) is the sum of Mo atoms and carbon atoms normalised over a single cell. The Mo_2C shows weak ferromagnetism, which is in agreement with experimental data [20]. As shown in the data, the total magnetic moment of the pristine Mo_2C structure mainly arises from the d-orbitals. The data for structure with C-Vacancy and Mo-Vacancy show slight changes compared to pristine Mo_2C. The MM data for C-Vacancy increased slightly while the MM for Mo-vacancy reduced slightly. The MM for structures with point doping shows a much more significant effect on MM than the cases for vacancies. A comparative analysis of magnetic moments in Mo_2C with various doped elements reveals different influences on magnetism. Ni, Co, Mn, V and Fe doping shows a significant increase in the MM, Cr shows a limited effect, while tungsten (W) shows a notable reduction in the magnetic moments.

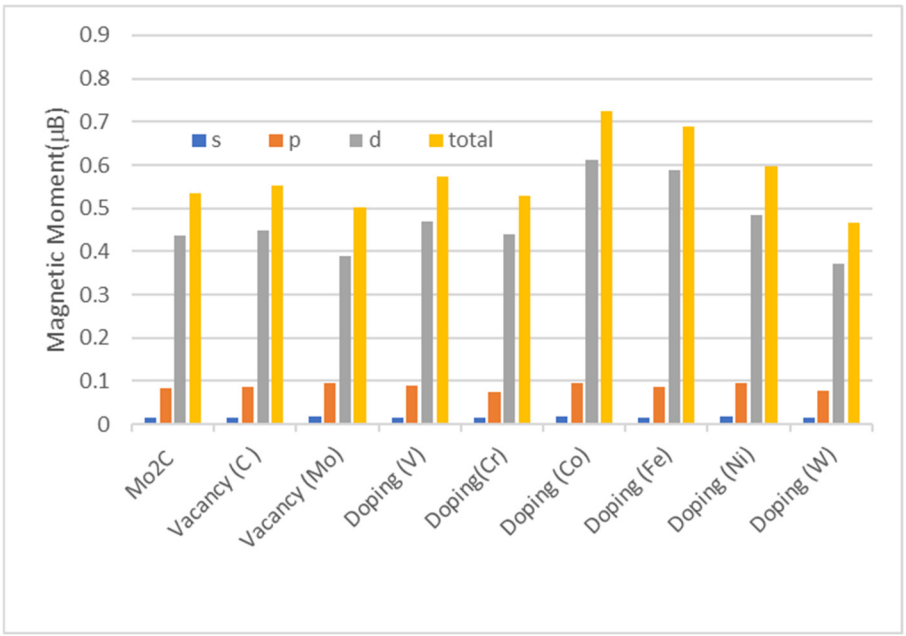

Figure 4. Effect of point defect on the magnetic moments (s. p. d represents the orbits).

As this work focuses on the effect of point defects, an important piece of data is the local magnetic moment of the doping atom in comparison with the Mo atom in the pristine structure, which is shown in Figure 5. When doping atoms are substituted into the Mo_2C lattice, these dopants display substantial influence on the local magnetic moment and characteristics. Vanadium (V) substitution produces a moderate magnetic moment of 0.342 μB at the dopant site, which is higher than that of the original Mo atom and W, but slightly lower than Ni and much lower than that of Fe and Co. This intermediate value is consistent with V's electron configuration, which allows for some unpaired electrons but lacks the strong magnetism with Fe or Co. Fe and Co substitutions introduce a significant increase in local magnetic moments compared to the MM in pristine Mo_2C. The elevated magnetic moments associated with Fe and Co dopants are in agreement with their known magnetic characteristics and suggest that these elements enhance the local magnetic interactions

within the Mo_2C lattice. The increased d-orbital contributions in these dopants to the total magnetic moments (as shown in Figure 4) indicate a strengthening of localised magnetic moments around the dopant sites, thereby enhancing the overall magnetic behaviour of the system. Chromium (Cr) substitution shows a slightly lower moment than Fe and Co. The data also clearly show that Ni has a reduced influence on local magnetism within the lattice. A notable trend is that tungsten (W) substitution results in relatively low magnetic moments at the dopant site. The lower magnetic moment for W is potentially attributed to its stable, less reactive electronic configurations, which result in weaker magnetic interactions with the surrounding Mo and C atoms.

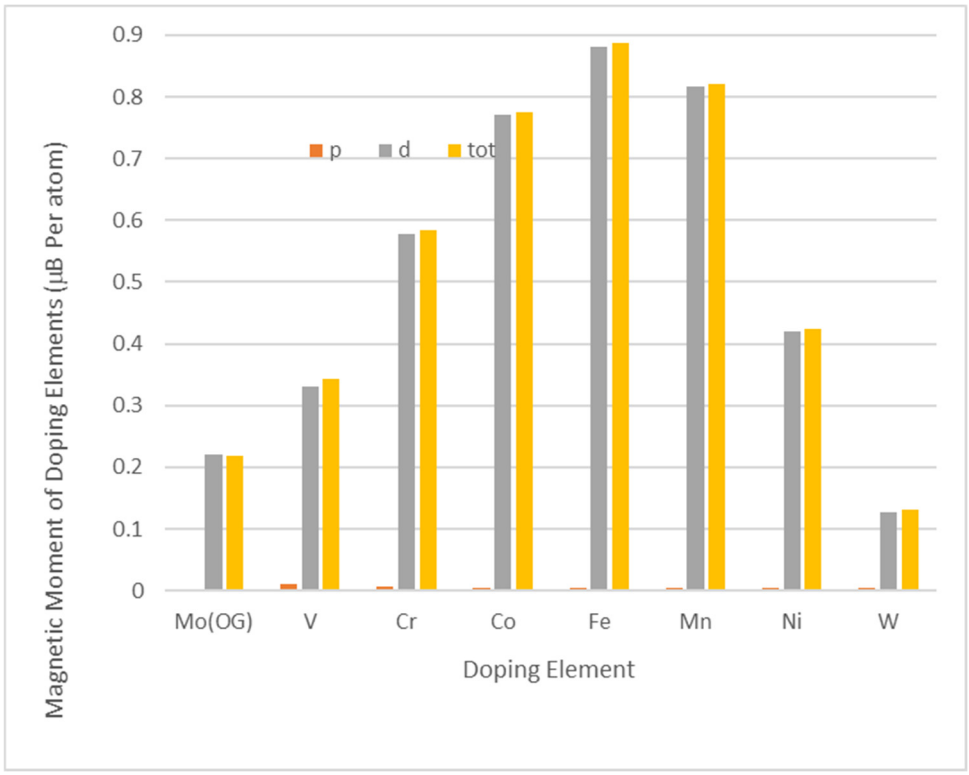

Figure 5. Local magnetic moment of individual doping atom. (OG: original. p. d represents the orbits. The data for 's-orbit' are not shown to preserve clarity.)

Figure 6 shows the band structure over the full spectrum and the density of state for Pristine Mo_2C, C-vacancy and Mo-vacancy, respectively. As shown in Figure 6a(i,ii), the defect-free Mo_2C structure shows spin splitting in the total density of states, indicating that the structure possesses spin polarization properties and some degree of magnetism as evident from the asymmetric electronic density of states in the total DOS up (TDOS) up and down orbits near the Fermi level. This distribution mainly originates from the electron contribution of the d orbital of Mo atoms. As shown in Figure 6b, the overall pattern of electronic structure changes significantly with the introduction of carbon vacancy. The spin polarization near the Fermi level is weakened, and the electronic density of states in the TDOS-down orbit is reduced. This finding indicates a redistribution of electrons around the vacancies to accommodate changes in local charge density, thus influencing the data for the magnetic moment. As shown in Figure 6c, upon removing a Mo atom, the band structure becomes slightly less dense near the Fermi level. The reduction in Mo d-states highlights the loss of critical conduction states due to the missing Mo atom. The change in symmetric feature between spin-up and spin-down states is not significant, consistent with limited change in the magnetic moments.

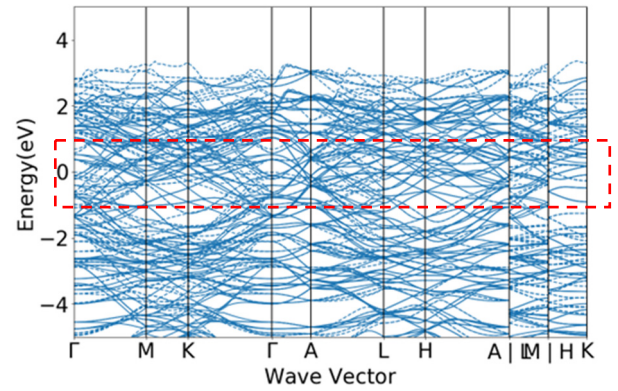

(**a**) (**i**) Pristine Mo_2C (Band Structure)

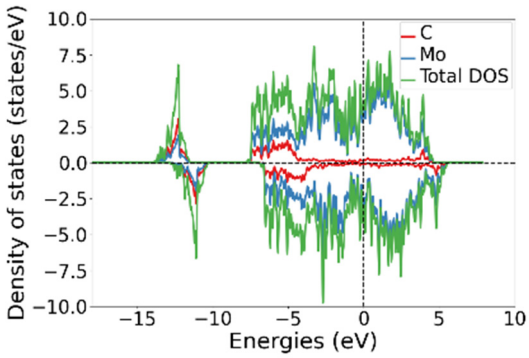

(**a**) (**ii**) Pristine Mo_2C (DOS)

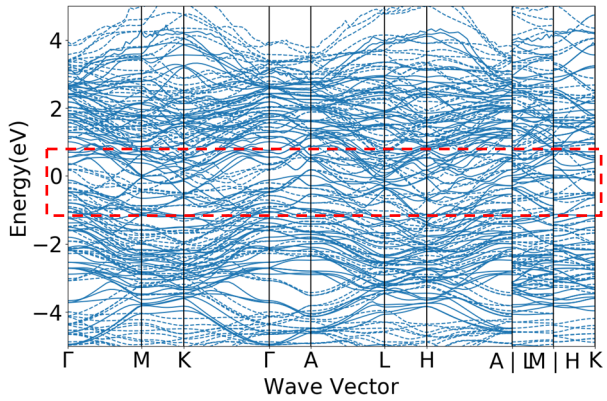

(**b**) (**i**) Mo_2C (C-Vacancy, Band Structure)

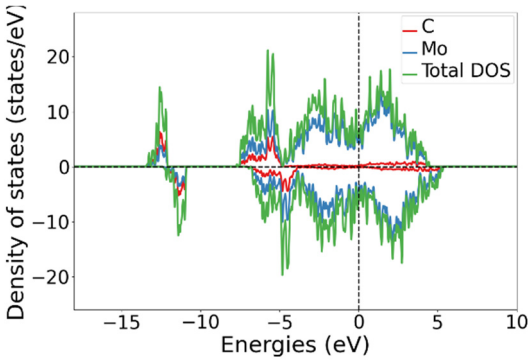

(**b**) (**ii**) Mo_2C (C-Vacancy, DOS)

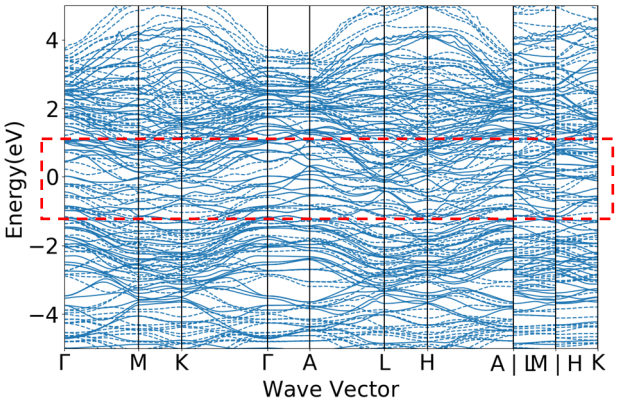

(**c**) (**i**) Mo_2C (Mo-Vacancy, Band Structure)

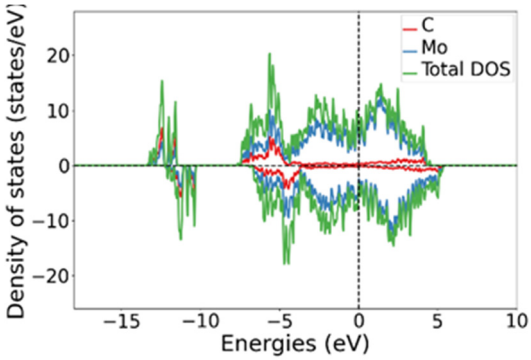

(**c**) (**ii**) Mo_2C (Mo-Vacancy, DOS)

Figure 6. Band structure (**i**) and DOS (**ii**) for Mo, C and total DOS of (**a**) Pristine Mo_2C, (**b**) C-Vacancy and (**c**) Mo-Vacancy. Γ (Gamma) is a special Brillouin zone high-symmetry point. The red dashed box highlights the main data of interest. These high-symmetry points (such as X, M, K, L, W, etc.) are chosen based on the crystal's symmetry and the geometry of the Brillouin zone. The Solid lines represent spin-up, dotted lines represent spin-down.

The key feature related to magnetic character with doping is reflected in the band structures. Figure 7 shows the band structure over the full range of spectrum for Mo_2C with different point doping elements. The band structure is an important piece of data providing critical insights into the electronic characteristics and their links to the effect of doping on magnetic and mechanical properties. Detailed analysis of data including spin band splitting at the Fermi level, band gap change, and enhancement of electron–electron interaction has been performed and comparatively analysed against the band structure of the Pristine Mo_2C (which is represented to make comparison easier). In general, the band

structure of crystals with doping is different from the pristine structure and those with vacancy defects. The energy band line density near the Fermi level varies depending on the dopant. The change in the spin-up and spin-down energy band represented by different colours indicates increased magnetic strength in the case of V, Fe, Co, Cr and Ni.

The different effects of the doping element on the DOS are shown in Figure 8. Compared to undoped Mo_2C, V-doping introduces more localised states near the Fermi level, manifested by an increase in the density of states above and below the Fermi level. This increased localised state reflects the influence of the d electrons of V atoms on the electronic structure of the system. There is an asymmetric distribution of spin-up (TDOS-UP) and spin-down (TDOS-DOWN) states observed near the Fermi level, correlating with an increase in the overall magnetism of the structure as shown by the change in the MM values (Figures 4 and 5). Analysis of the data for other elements (Co, Ni, Fe, Cr) shows notable deviations from the DOS of pristine Mo_2C near the Fermi level with more asymmetric distribution of spin-up (TDOS-UP) and spin-down (TDOS-DOWN) states. This correlates well with the magnetic moment data trend. W doping shows the overall impact on the electronic structure around the energy level and the distribution of states, but there is no significant change in the spin density around the Fermi level compared to the pristine structure. This means that tungsten doping has minimal influence on the material's magnetic properties, which agrees with the results shown in Figures 4 and 5.

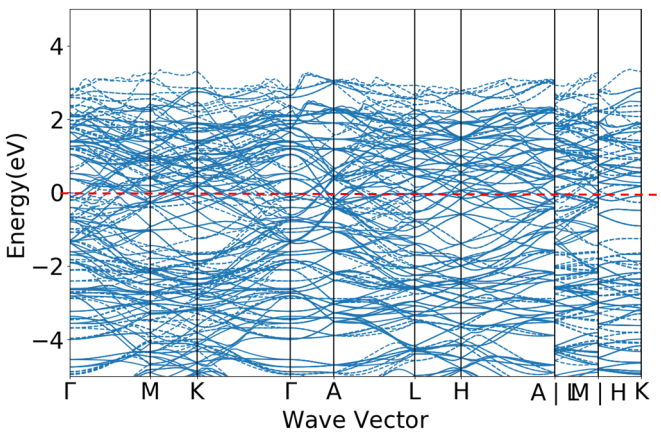

(**a**) Pristine Mo_2C

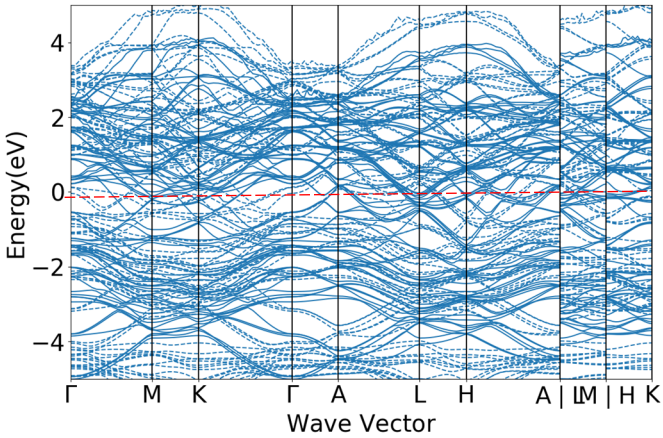

(**b**) Doping $S_{V\text{-}Mo}$

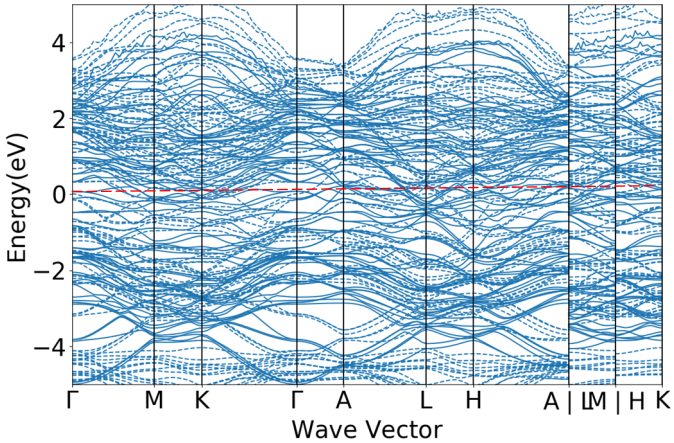

(**c**) Doping $S_{Co\text{-}Mo}$

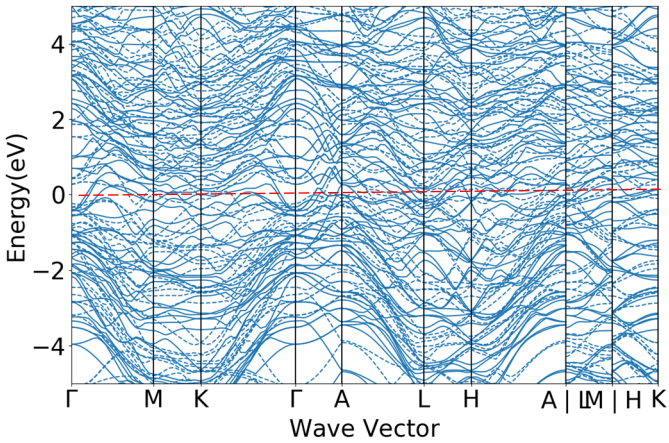

(**d**) Doping $S_{Fe\text{-}Mo}$

Figure 7. *Cont.*

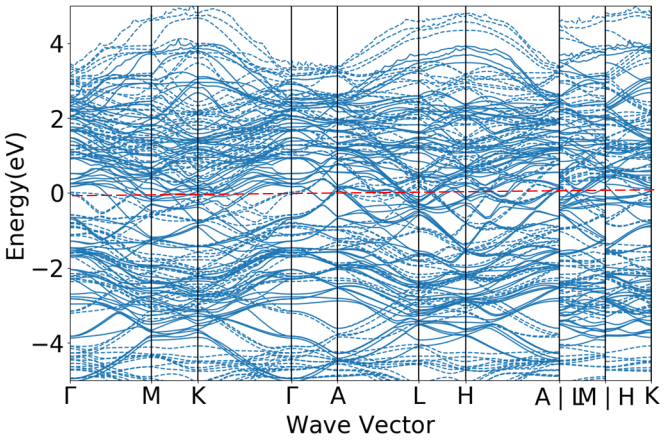

(**e**) Doping $S_{Cr\text{-}Mo}$

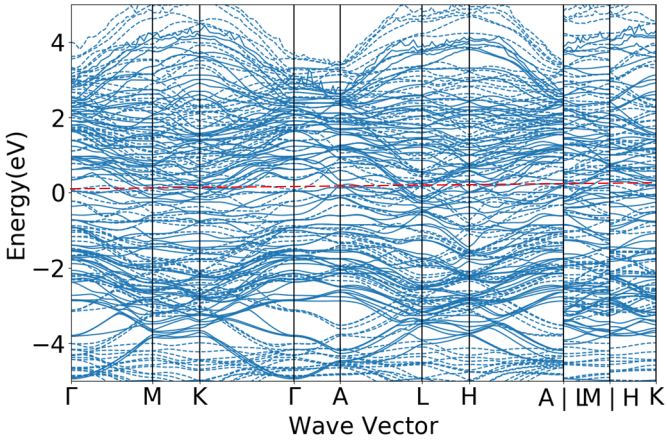

(**f**) Doping $S_{Ni\text{-}Mo}$

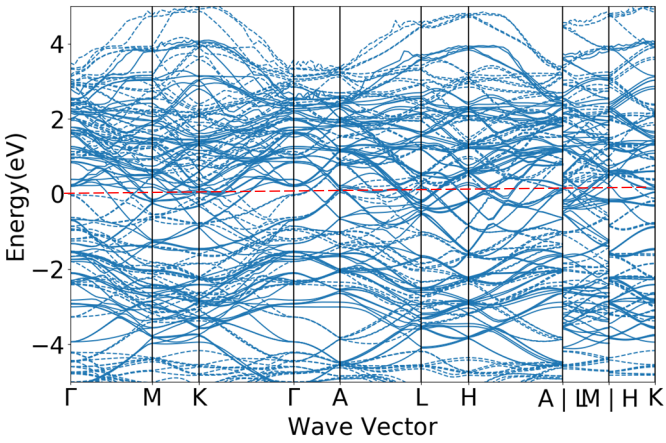

(**g**) Doping $S_{W\text{-}Mo}$

Figure 7. The electronic band structures for Mo_2C with different doping elements. Γ (Gamma) is a special Brillouin zone high-symmetry point. These high-symmetry points (such as X, M, K, L, W, etc.) are chosen based on the crystal's symmetry and the geometry of the Brillouin zone. The Solid lines represent spin-up, dotted lines represent spin-down.

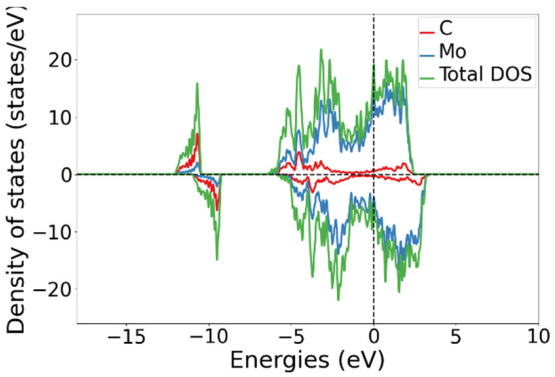

(**a**) Pristine Mo_2C

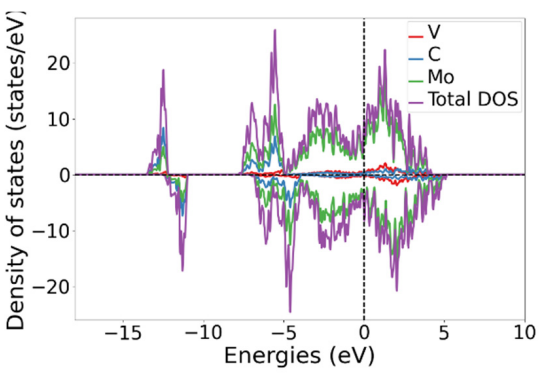

(**b**) Doping (V) $S_{V\text{-}Mo}$

Figure 8. *Cont.*

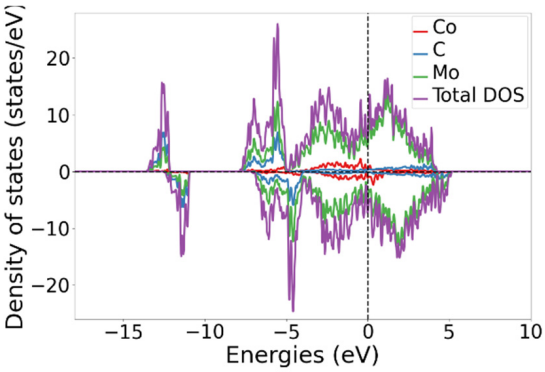

(**c**) Doping (Co) $S_{Co\text{-}Mo}$

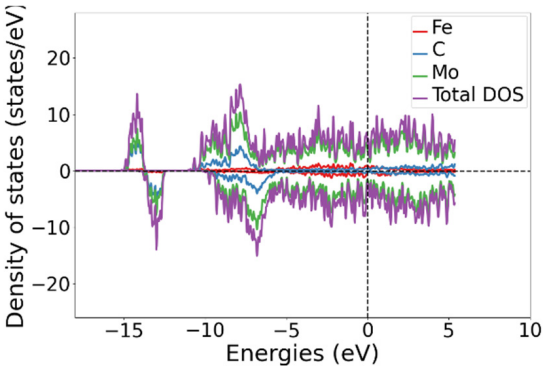

(**d**) Doping (Fe) $S_{Fe\text{-}Mo}$

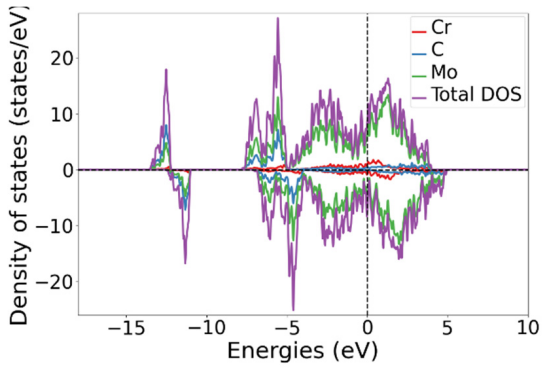

(**e**) Doping (Cr) $S_{Cr\text{-}Mo}$

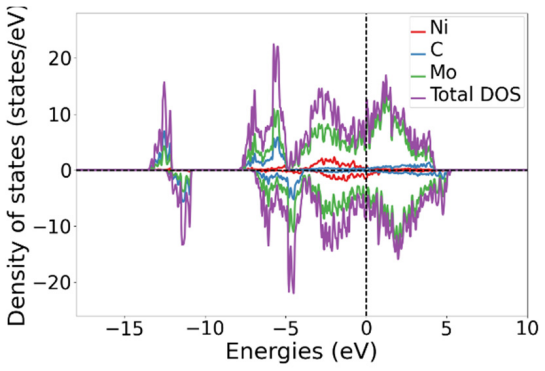

(**f**) Doping (Ni), $S_{Ni\text{-}Mo}$

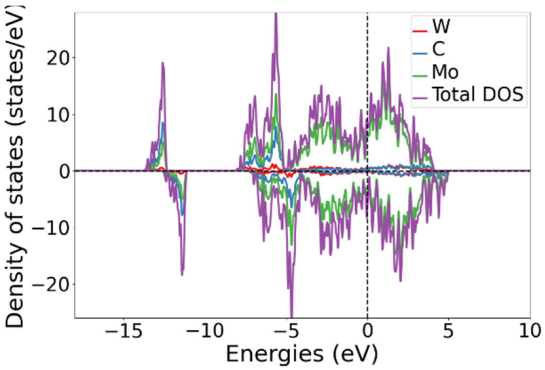

(**g**) Doping (W), $S_{W\text{-}Mo}$

Figure 8. Density of total states (DOS) analysis of Mo_2C with different doping elements. (All the lines for the doping elements are plotted in red in (**b**–**g**)).

4. Discussions

This is paper focus on the comparative data development and analysis of Mo_2C with point defects, including vacancy and substitutional doping of a range of metal elements. The development of the models and assessment follow similar approaches [2,3,13,20,23,33]. These results indicate that for all cases (Figures 4 and 5), d-electron states play a dominant role in the material's intrinsic magnetic moment. A combined analysis of the total and local magnetic moments for different doping elements revealed the trend showing that dopants with higher unpaired d-electrons, such as Fe and Co, are more effective at enhancing the magnetic properties of Mo_2C. Elements like V, Ni and Cr also shows clear influence on the magnetic moment with a smaller scale. These reflect the known stronger magnetic characteristics of Fe and Co elements. The magnetic moment for W is lower than the

original Mo atom, contributing less to the magnetic behaviour, which is probably due to their stable, lower-magnetisation electronic configurations. Some of the data also showed a reasonable agreement on the trend with experimental findings [20,44]. For example, Dantas et al. [20] investigated the magnetic feature of Mo_2C and Ni-doping demonstrated an enhancement in the ferromagnetic properties of Mo_2C. The systematic data set presented here facilitates comparison and highlights the main trends among substitutional doping effects on magnetic moment data. These trends correlate with other parameters such as the Mulliken atomic charge, bond population and DOS data for different doping elements.

Apart from the magnetic data presented (Figures 5 and 6), point defects and doping are known linked to properties such as bulk modulus. As a reliable measurement of volumetric elasticity, bulk modulus closely correlates to other non-elastic properties, such as hardness, toughness and potentially with local magnetic behaviours [17,19,49]. The bulk modulus can be calculated from DFT results by using the equation: $K = -V(dP/dV)$, where B is the bulk modulus, V is the volume and dP/dV is the derivative of pressure with respect to volume. The elastic calculation is performed after the structure relaxation, the stiffness tensor matrix is determined

$$C_{ij}^{cubic} = \begin{pmatrix} C_{11} & C_{12} & C_{12} & 0 & 0 & 0 \\ C_{12} & C_{11} & C_{12} & 0 & 0 & 0 \\ C_{12} & C_{12} & C_{11} & 0 & 0 & 0 \\ 0 & 0 & 0 & C_{44} & 0 & 0 \\ 0 & 0 & 0 & 0 & C_{44} & 0 \\ 0 & 0 & 0 & 0 & 0 & C_{44} \end{pmatrix} \quad (9)$$

The Voigt bounds are given by the following equations:

$$9K_V = (C_{11} + C_{22} + C_{33}) + 2(C_{12} + C_{23} + C_{31}) \quad (10)$$

while the Reuss bounds are given by:

$$1/K_R = (S_{11} + S_{22} + S_{33}) + 2(S_{12} + S_{23} + S_{31}) \quad (11)$$

Figure 9 shows the bulk modulus of Mo_2C with various point defects. It shows a significant change in the bulk modulus with different doping elements. The bulk modulus of the Mo_2C agrees well with some published data (294–302 GPa) [23,45]. As shown in the data, the vacancies of C and Mo reduce the bulk modulus, which is consistent with reported trend that vacancies bulk modulus and increase ductility [7]. It is noted that the effect of doping reveals an opposite effect on the bulk modulus (Figure 9) and magnetic moments (Figures 4 and 5). The effect of point doping shows a different trend among the elements studied. Co, Fe, Cr and Ni all reduce the bulk modulus, while V and W slightly increase it.

Compared to the effect of doping elements on magnetic moments in Figures 4 and 5, W shows less effect on the MM but a more significant increase in the bulk modulus. In contrast, other elements exhibit an increased magnetic moment but a reduced bulk modulus. The link between magnetism and bulk modulus is an important but complex issue, which could be affected by structural, electronic and bonding situations, magnetic conditions and size of the dopant [50,51]. Liu et al. [50] proposed a bulk modulus model for crystal materials based on the bond valence model. Gueddouh et al. [49] studied the correlation between the magnetic moment and bulk modulus of $Fe_{(1-x)}Mn_xB$ with different Mn contents. Recently, Jin et al.'s work [52] reported on atomic strength for bulk modulus prediction and high-throughput screening of ultra-incompressible crystals. Data such as band population and band structures could provide some useful data directly or indirectly linked to both magnetic characteristics and bulk modulus. As shown in Figure 10, there

is a clear difference in some parts with band structure of the pristine Mo_2C, C-Vacancy, Mo-Vacancy and V-doping and W doping. The results show changes in the overall pattern of the energy band and distributions, asymmetrical nature of up and down energy band, and the density of energy bands near the Fermi level, indicating the change in bonding conditions. The detailed role of some key factors such as effective valence and positive bond population on the covalency of crystalline solids remains an active area of research and exploration [47,51]. The comparative data for different doping elements presented in this study will be used for future quantitative analysis to identify the most influential factors on bonding, covalency and related properties.

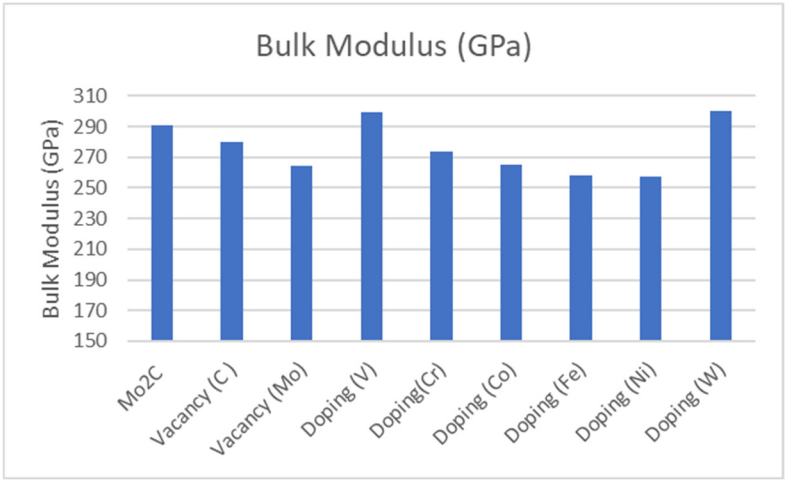

Figure 9. The bulk modulus of Mo_2C with different point defects.

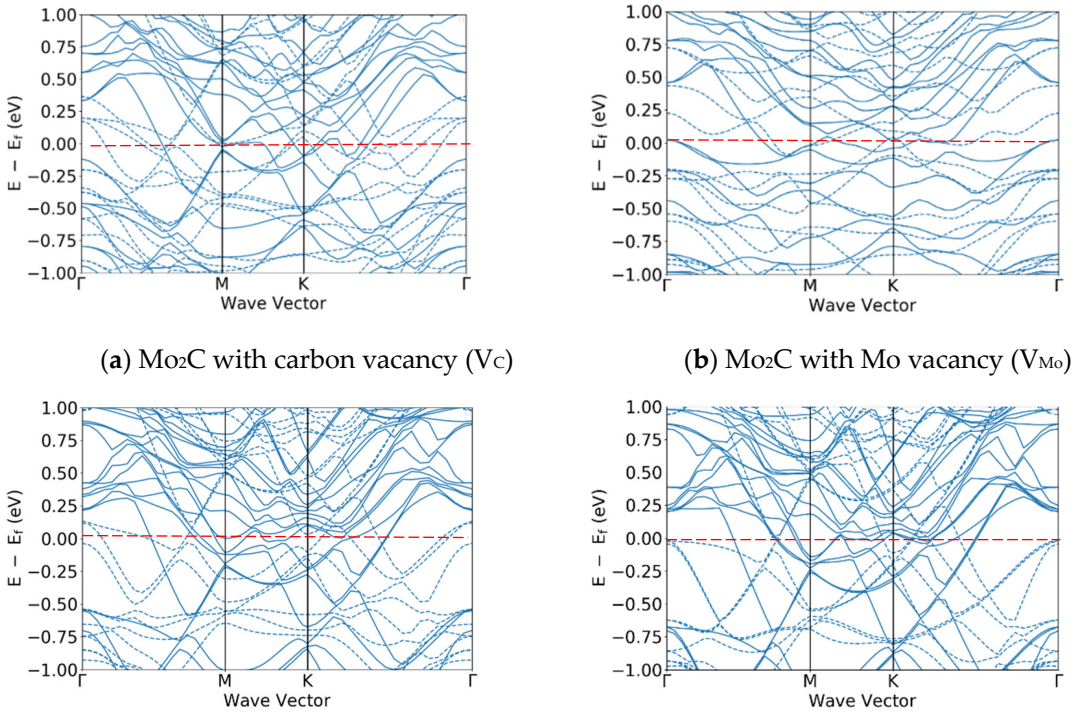

(**a**) Mo_2C with carbon vacancy (V_C)

(**b**) Mo_2C with Mo vacancy (V_{Mo})

(**c**) Mo_2C with V doping ($S_{V\text{-}Mo}$)

(**d**) Mo_2C with W doping ($S_{W\text{-}Mo}$)

Figure 10. Comparison of the band structure between Mo_2C with Carbon vacancy (**a**), Mo vacancy (**b**), V doping (**c**) and W doping (**d**). Γ (Gamma) is a special Brillouin zone high-symmetry point. These high-symmetry points (such as M, K,) are chosen based on the crystal's symmetry and the geometry of the Brillouin zone, solid lines represent spin-up, and dotted lines represent spin-down.

Another important aspect of the fundamental understanding of the effects of point defects and the interlink between magnetic and mechanical properties is the comparative studies of data for 3D and 2D structures. Two-dimensional Mo_2C as a monolayer is increasingly being used and/or explored in areas such as energy and catalyst applications [53–55]. Doping of a small amount of other metal elements could be an effective way of tuning properties, as both the magnetic and mechanical properties are crucial for enhanced magnetic performance [21]. Figure 11 shows some typical magnetic moment data of a Mo_2C monolayer with different doping [43]. The overall trend of the effect of doping elements on magnetic moment is similar to that of the 3D Mo_2C (as shown in Figures 4 and 5). Given the monolayer's potential application in energy and catalysts, enhancement of the magnetic properties is important. Other factors, such as strain, are also relevant to 2D structures, which will be addressed in future studies [43].

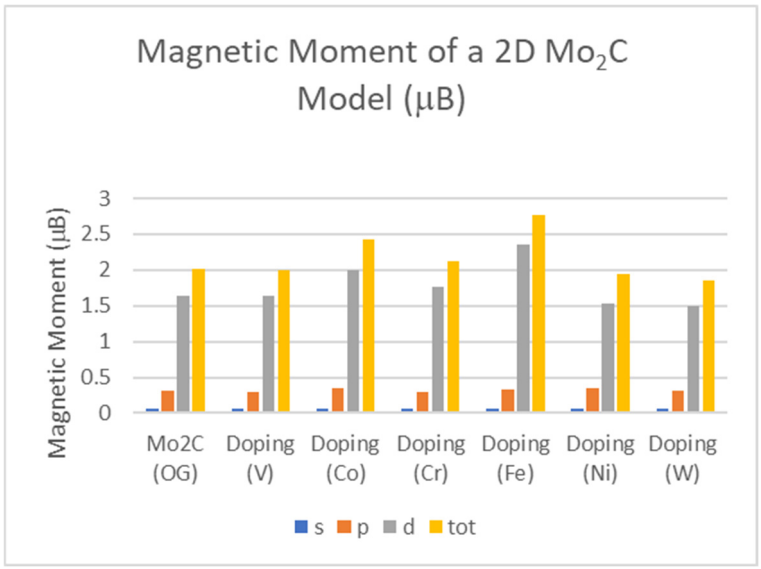

Figure 11. Data showing the effect of substitutional doping on the magnetic moment of Mo_2C monolayers model (Mo_7MC_4).

As shown in selected data and other published works [3,19,24,33], first-principles calculations are an effective tool for developing grand state data of crystals with different point defects, which are crucial for understanding the properties of materials used as bulk or 2D structures. DFT calculation is also an effective means for providing complex data for enhancing the understanding of different mechanisms and developing approaches to tune or enhance the magnetic properties. An effective approach to establishing the ground state magnetic and other related properties helps in understanding how materials respond to different external factors, such as temperature, pressure, etc. [56]. Apart from the applications directly linked to magnetic properties, such as energy and catalyst, the knowledge is also essential for studying the material's behaviour and predicting its behaviour under various conditions in material processing such as the magnetism and high magnetic-field-induced stability of alloy carbides in complex in alloys (Fe, Ni, Cr, V etc.) [17]. Understanding the role of controlled substitutional point doping will also provide data for understanding the complex defects and developing multicomponent carbides including phase transformation. In previous work, DFT data were used to analyse the potential transition from Mo_2C to $(Mo, V)_2C$ [3]. Some recent works also highlighted the potential impact of DFT in this area. For example, DFT data have been used to analyse the formation/transformation of different key phases such as multicomponent compounds (e.g., carbides in steels and other alloys) [6,8,12,17,19,32]. In a very recent work by Khatri et al. [13], first-principles predic-

tions were used to predict point defect energies and concentrations in the tantalum and hafnium carbides. Future work will be focused on the use of first-principles calculations to provide systematic predictive data for enhancing the understanding of key mechanisms controlling properties and tuning the mechanical, physical or functional properties of 3D or 2D structures [16,34]. For example, the data in Table 1 for the effect of the point vacancies and doping elements on the lattice parameters are new data to analyse the probability of the carbides acting as a potential nucleation site of another metallic phase (e.g., ferrite or austenite) or other compounds in materials process, such as welding, which is an important R&D area in materials [57]. Detailed data-driven comparative studies on the synergy of different properties are important for both R&D related to crystals and collaborative interdisciplinary training in the use of DFT in materials development [24,25,32,58–60].

5. Conclusions

In this study, the first-principles method is applied to comparatively study the effects of point vacancies and different substitutional doping on the structures, and electronic, magnetic and mechanical properties of Mo_2C, and the correlation between magnetic properties in 3D and 2D structures. The data for lattice structure changes and Mulliken atomic charge and bond population associated with different defects were developed. The dopant-specific local magnetic moments and total magnetic contributions indicate that dopants with higher unpaired d-electrons, such as Fe and Co, are more effective at enhancing the magnetic properties of Mo_2C. V and Ni shows a moderate enhancement of the magnetic moment. The magnetic moment for W-doped Mo_2C is lower than pristine phase due to their stable, lower magnetization electronic configurations. The comparison between the data for 3D and 2D Mo_2C structures showed that doping elements have a similar effect on the magnetic moment. The comparison between magnetic and mechanical data showed that the doping element has the opposite effect on magnetic moments and the bulk modulus in Mo_2C. The potential use of the DFT data related to point defects and doping in the R&D of materials processing and future directions is discussed.

Author Contributions: Conceptualization, X.Q., Q.Y., and X.R.; methodology, X.Q., J.G., X.L., Q.Z., L.W., C.T., T.K., and X.Q.; formal analysis and investigation, J.G., L.W., and X.R.; writing—original draft preparation, X.Q., Q.Y., and X.R.; writing—review and editing, L.W., X.L., X.Q., and N.O.; supervision, Q.Y., L.W., and X.R.; project administration and funding acquisition, X.R., L.W., and Q.Y. All authors have read and agreed to the published version of the manuscript.

Funding: This research was funded by The European Union's Horizon 2020 Research and Innovation Programme under the Marie Skłodowska-Curie grant agreement (No. 823786, 101129996) and UKRI Project EP/Y036867/1.

Data Availability Statement: The data presented in this study are available on request from the corresponding authors.

Conflicts of Interest: The authors declare no conflicts of interest.

References

1. Razumovskiy, V.I.; Popov, M.N.; Ding, H.; Odqvist, J. Formation and interaction of point defects in group IVb transition metal carbides and nitrides. *Comput. Mater. Sci.* **2015**, *106*, 155–163. [CrossRef]
2. Yang, J.; Xiao, Z.; Li, Z.; Wen, Q.; Yang, F. First principles study on the structural, electronic and magnetic properties of Ni_4C. *Comput. Condens. Matter* **2014**, *1*, 3364–3370. [CrossRef]
3. Guo, J.; Feng, Y.; Tang, C.; Wang, L.; Qing, X.; Yang, Q.; Ren, X. Insight into Point Defects and Complex Defects in β-Mo_2C and Carbide Evolution from First Principles. *Materials* **2022**, *15*, 4719. [CrossRef]
4. Zhang, H.; Lou, Y.; Wu, D.; Liao, Y.; Xie, J. Tuning the magnetic properties of double transition-metal carbide CoMC (M = Ti, V, Cr, Mn, Fe, Ni) monolayers. *Phys. Chem. Chem. Phys.* **2024**, *26*, 12681–12697. [CrossRef] [PubMed]

5. Zhang, H.; Hu, T.; Wang, X.; Li, Z.; Hu, M.; Wu, E.; Zhou, Y. Discovery of carbon-vacancy ordering in Nb_4AlC_{3-x} under the guidance of first-principles calculations. *Sci. Rep.* **2015**, *5*, 14192.
6. Sun, C.; Zheng, Y.; Fang, F. Optimization of thermal stability and mechanical properties of Mo2C carbides via multi-element doping: Experimental and theoretical calculations. *J. Mater. Sci.* **2022**, *57*, 16352–16366. [CrossRef]
7. Bai, Y.; Liang, Y.; Bi, J.; Cuyi, B.; Lu, Z.; Li, B. Role of carbon vacancies in determining the structural, mechanical, and thermodynamic properties of (HfTaZrNb)C1-x high entropy carbides: A first-principles study. *J. Mater. Sci.* **2024**, *59*, 19112–19124. [CrossRef]
8. Bie, X.; Hou, J.; Zhou, X.; Song, J. Sub-stoichiometry and vacancy structures in V/Nb carbide precipitates by cluster expansion and first-principles calculations. *Acta Mater.* **2024**, *242*, 119806. [CrossRef]
9. Cao, Y.; Tan, Y.; Zhu, X.; Li, H.; Zhao, Y. Enhanced N2 fixation on V2C by transition metal doping (Fe, Co, Mo, Ru). *Phys. E Low-Dimens Syst. Nanostruct.* **2021**, *134*, 114875. [CrossRef]
10. Cheng, W.; Li, C.; Wang, T.; Cheng, S.; Gao, N.; Li, H. Electronic and magnetic properties of Au-doped diamond surfaces by first-principles calculation. *Phys. Chem. Chem. Phys.* **2024**, *26*, 1436. [CrossRef]
11. Xiang, S.; Ma, L.; Yang, B.; Dieudonne, Y.; Pharr, G.M.; Lu, J.; Yadav, D.; Hwang, C.; LaSalvia, J.C.; Haber, R.A.; et al. Tuning the deformation mechanisms of boron carbide via silicon doping. *Sci. Adv.* **2019**, *5*, eaay0352. [CrossRef] [PubMed]
12. Feng, Q.; Li, J.; Zeng, Y.; Wang, Y.; Wang, Y.; Liu, B.; Tang, G. Effect of Cr atom doping on the carbide stability and mechanical properties of high carbon chromium bearing steels. *J. Mater. Res. Technol.* **2023**, *24*, 2543–2552. [CrossRef]
13. Khatri, I.; Koju, R.K.; Mishin, Y. First-principles prediction of point defect energies and concentrations in the tantalum and hafnium carbides. *Acta Mater.* **2024**, *242*, 120216. [CrossRef]
14. Shah, N.K.; Kaphle, G.C.; Karn, A.L.; Limbu, Y.; Paudyal, D. Interplay of electronic structure, magnetism, strain, and defects in carbide MXenes. *Vacuum* **2022**, *200*, 111489. [CrossRef]
15. Hui, L.; Chen, Z.Q.; Xie, Z. Stability, magnetism and hardness of Iron carbides from first-principles calculations. *J. Supercond. Nov. Magn.* **2018**, *31*, 353–364. [CrossRef]
16. Malik, A.; Rohrer, J.; Karsten Able, K. Theoretical study of thermodynamic and magnetic properties of transition metal carbide and nitride MAX phases. *Phys. Rev. Mater.* **2023**, *7*, 044408. [CrossRef]
17. Hou, T.P.; Li, Y.; Zhang, J.J.; Wu, K.M. Effect of magnetic field on the carbide precipitation during tempering of a molybdenum-containing steel. *J. Magn. Magn. Mater.* **2012**, *324*, 857–861. [CrossRef]
18. Hou, T.P.; Li, Y.; Wu, K.; Peet, M.; Hulme-Smith, C.; Guo, L. Magnetic-field-induced magnetism and thermal stability of carbides Fe6-xMoxC in molybdenum-containing steels. *Acta Mater.* **2016**, *102*, 24–31. [CrossRef]
19. Zhang, D.; Hou, T.; Liang, X.; Zheng, P.; Luo, W.; Lin, H.; Xiao, X.; Wu, K. Insights into the assessment of the magnetic-field-induced precipitation behavior of alloy carbides M7C3 in steels. *Mater. Des.* **2022**, *221*, 111023. [CrossRef]
20. Dantas, S.L.A.; Souza, A.L.R.; Bohn, F.; Lopes-Moriyama, A.L.; Souza, C.P.; Correa, M.A. Magnetic properties of Ni-doped Mo_2C produced by fixed bed reactor. *Mater. Lett.* **2020**, *277*, 127916. [CrossRef]
21. Xie, J.; Wu, D.; Liao, Y.; Cao, X.; Zhou, S. Tuning the magnetic properties of nonmagnetic monolayer Mo_2C by doping and adsorption. *Phys. B Condens. Matter* **2023**, *667*, 415219. [CrossRef]
22. Yang, J.; Pang, X.; Pang, M.; Zhao, Y.; Yang, W.; Zhan, Y. Understanding the influence of rare earth yttrium on surface characterizations of orthorhombic α-Mo_2C(023) surface: A first-principle calculation approach. *Surf. Sci.* **2021**, *708*, 121823. [CrossRef]
23. Liu, X.; Zhou, X.; Yang, M. First-principles calculation of structural stability and mechanical properties of Cr doped Mo_2C carbide. *J. Mater. Sci.: Mater. Electron.* **2023**, *34*, 961.
24. Leitner, S.; Scheiber, D.; Dengg, T.; Spitaler, T.; Antretter, T.; Ecker, W. Analysis of shape, orientation and interface properties of Mo_2C precipitates in Fe using ab-initio and finite element method calculations. *Acta Mater.* **2021**, *204*, 116478. [CrossRef]
25. Kameya, M.; Taniguchi, S.; Kobayashi, Y.; Matsui, N.; Yamasaki, S. Carbide precipitation and hydrogen trapping behavior in Mo and V added tempered martensitic steel. *ISI J. Int.* **2024**, *64*, 645–654. [CrossRef]
26. Wang, X.R.; Yan, M.F.; Chen, H.T. First-Principles Calculations of Hardness and Melting Point of Mo_2C. *J. Mater. Sci. Technol.* **2009**, *25*, 419–422.
27. Razumovskiy, V.I.; Ghosh, G. A first-principles study of cementite (Fe_3C) and its alloyed counterparts: Structural properties, stability, and electronic structure. *Comput. Mater. Sci.* **2015**, *110*, 172–180.
28. Karaca, E.; Bağcı, S.; Tütüncü, H.M.; Uzunok, H.Y.; Srivastava, G.P. Theoretical investigation of electron-phonon interaction in the orthorhombic phase of Mo_2C. *J. Alloys Compd.* **2019**, *788*, 842–851. [CrossRef]
29. Hugosson, H.; Eriksson, O.; Nordström, L.; Jansson, U.; Fast, L.; Delin, A.; Wills, J.; Johansson, B. Theory of phase stabilities and bonding mechanisms in stoichiometric and substoichiometric molybdenum carbide. *J. Appl. Phys.* **1999**, *86*, 3758–3767. [CrossRef]
30. Wang, Q.; Mi, F.; Li, J.; Wu, Y.; Zhou, X.; Ma, G.; Ren, S. Tungsten doping generated Mo_2C-MoC heterostructure to improve HER performance in alkaline solution. *Electrochim. Acta* **2021**, *370*, 137796. [CrossRef]

31. Tao, L.; Huang, L.; Pang, K.; Li, C.; Ji, H. Fe-doped Mo_2C for boosting electrocatalytic N_2 reduction. *Inorg. Chem. Commun.* **2022**, *145*, 110003. [CrossRef]
32. Cheng, S.; Hou, T.; Zhang, D.; Wang, Z.; Yin, C.; Pan, X.; Liu, X.; Hu, S.; Wu, K. New insights into the formation mechanism of the multicomponent carbides (Nb, M)C (M = Ti, Cr, and Mn). *J. Mater. Res. Technol.* **2023**, *25*, 10234–10248. [CrossRef]
33. Guo, J.; Feng, Y.; Tang, C.; Ren, X. Intrinsic defects, Mo-related defects, and complexes in transition-metal carbide VC: A first-principles study. *J. Am. Ceram. Soc.* **2020**, *103*, 7226–7239. [CrossRef]
34. Patnaik, P.; Das, D.K.; Panda, S.; Mukhopadhyay, G. Substitutional tungsten doping in silicon carbide introducing magnetic properties: A computational DFT approach. *Curr. Phys. Chem.* **2022**, *12*, 53–59.
35. Tellez-Mora, A.; He, X.; Bousquet, E. Systematic determination of a material's magnetic ground state from first principles. *npj Comput. Mater.* **2024**, *10*, 20. [CrossRef]
36. Kresse, G.; Furthmüller, J. Efficient iterative schemes for ab initio total-energy calculations using a plane-wave basis set. *Phys. Rev. B* **1996**, *54*, 11169. [CrossRef]
37. Liu, J.C.; Zhu, Z.H.; Lai, R.D.; Zhao, H.D. A first-principles study on structural and electronic properties of Mo_2C. *Scripta Mater.* **2009**, *60*, 949–952. [CrossRef]
38. Sun, H.; Xu, Z.; Zhang, D. First-principles calculations to investigate doping effects on electrical conductivity and interfacial contact resistance of TiO_2. *Appl. Surf. Sci.* **2022**, *599*, 156202.
39. Perdew, J.P.; Burke, K.; Ernzerhof, M. Generalized Gradient Approximation Made Simple. *Phys. Rev. Lett.* **1996**, *77*, 3865. [CrossRef]
40. Blöchl, P.E. Projector augmented-wave method. *Phys. Rev. B* **1994**, *50*, 17953. [CrossRef] [PubMed]
41. Gaillac, R.; Pullumbi, P.; Coudert, F.-X. ELATE: An open-source online application for analysis and visualization of elastic tensors. *J. Phys. Condens. Matter* **2016**, *28*, 275201. [CrossRef] [PubMed]
42. Duan, J.; Hou, T.; Zhang, D.; Wu, K. Insights to the fracture toughness, damage tolerance, electronic structure, and magnetic properties of carbides M_2C (M = Fe, Cr). *Mater. Res. Express* **2023**, *10*, 046515. [CrossRef]
43. Qing, X. Predictive Modelling and Analysis of Complex Carbides Based on First Principles Calculation and Molecule Dynamics. Ph.D. Thesis, Liverpool John Moores University, Liverpool, UK, 2024. *In process*.
44. Wilson, A. (Ed.) *Structure Reports*; International Union of Crystallography (IUCR): Chester, UK, 1952; Volume 16.
45. Liu, Y.Z.; Jiang, Y.H.; Zhou, R.; Liu, X.F.; Feng, J. Elastic and thermodynamic properties of Mo_2C polymorphs from first principles calculations. *Ceram. Int.* **2015**, *41*, 5239–5246. [CrossRef]
46. Chong, X.; Jiang, Y.; Zhou, R.; Feng, J. The effects of ordered carbon vacancies on stability and thermo-mechanical properties of V_8C_7 compared with VC. *Sci. Rep.* **2016**, *23*, 34007. [CrossRef] [PubMed]
47. Hadi, M.; Christopoulos, S.; Chroneos, A.; Naqib, S.; Islam, A.K.M.A. DFT insights into the electronic structure, mechanical behaviour, lattice dynamics and defect processes in the first Sc-based MAX phase Sc_2SnC. *Sci. Rep.* **2022**, *12*, 14037. [CrossRef]
48. Ganguly, A.; Murthy, V.; Kannoorpatti, K. Structural and electronic properties of chromium carbides and Fe-substituted chromium carbides. *Mater. Res. Express* **2020**, *7*, 056508. [CrossRef]
49. Gueddouh, A.; Benghia, A.; Maabed, S. Effect of Mn content in $Fe_{1-x}Mn_xB$ (x = 0, 0.25, 0.5, 0.75, and 1) on physical properties—Ab initio calculations. *Mater. Sci.-Pol.* **2019**, *37*, 71–82. [CrossRef]
50. Liu, X.; Wang, H.; Wang, W.; Fu, Z. A simple bulk modulus model for crystal materials based on the bond valence model. *Phys. Chem. Chem. Phys.* **2017**, *19*, 22177–22189. [CrossRef] [PubMed]
51. Özdogan, K.; Galanakis, L. Interplay between structural, electronic, and magnetic properties in the p^0-d Semi-Heusler compounds: The case of Li-based compounds. *Crystals* **2024**, *14*, 693. [CrossRef]
52. Jin, R.; Yuan, X.; Gao, E. Atomic stiffness for bulk modulus prediction and high-throughput screening of ultra-incompressible crystals. *Nat. Commun.* **2023**, *14*, 4258. [CrossRef] [PubMed]
53. Jalil, A.; Sun, Z.; Wang, D.; Wu, X. Magnetic and electronic properties of single-walled Mo_2C nanotube: A first-principles study. *J. Phys. Condens. Matter* **2018**, *30*, 155305. [CrossRef]
54. Lou, H.; Yu, T.; Ma, J.; Zhang, S.; Bergara, A.; Yang, G. Achieving high hydrogen evolution reaction activity of a Mo_2C monolayer. *Phys. Chem. Chem. Phys.* **2020**, *22*, 26189–26199. [CrossRef] [PubMed]
55. Wu, J.; Su, J.; Wu, T.; Huang, L.; Li, Q.; Luo, Y.; Jin, H.; Zhou, J.; Zhai, T.; Wang, D.; et al. Scalable synthesis of 2D Mo_2C and thickness-dependent hydrogen evolution on its basal plane and edges. *Adv. Mater.* **2023**, *35*, 2209954. [CrossRef]
56. Hou, T.P.; Wu, K.M.; Liu, W.M.; Peet, M.J.; Hulme-Smith, C.N.; Guo, L.; Zhuang, L. Magnetism and high magnetic-field-induced stability of alloy carbides in Fe-based materials. *Sci. Rep.* **2018**, *8*, 3049. [CrossRef]
57. Song, W.; He, Q.; Rao, L.; Zhang, S.; Wang, J.; Ren, J.; Yang, Q.I. Heterogeneous nucleation interface between $LaAlO_3$ and niobium carbide: First-principles calculation. *Appl. Surf. Sci.* **2022**, *606*, 154731. [CrossRef]
58. Ye, T.; Lin, L.; Ruan, Z.; Fan, T.; Wu, Y.; Chen, D. The influence of substitutional defects of transition metal elements on the stability and thermal properties of Al at finite temperatures: A first-principles study. *Crystals* **2024**, *14*, 35. [CrossRef]

59. Shao, H.; Qiu, J.; Liu, X.; Hou, X.; Zhang, J. The temperature-dependent thermal conductivity of C- and O-doped Si_3N_4: First-principles calculations. *Crystals* **2024**, *14*, 549. [CrossRef]
60. Li, X.; Zhang, X.; Qin, J.; Zhang, S.; Ning, J.; Jing, R.; Ma, M.; Liu, R. First-principles calculations of structural stability and mechanical properties of tungsten carbide under high pressure. *J. Phys. Chem. Solids* **2014**, *75*, 1234–1239. [CrossRef]